

Application of Ultra-Wideband Synthesis in Software Defined Radar for UAV-based Landmine Detection

Samuel Prager* and Mahta Moghaddam†

*sprager@usc.edu, †mahta@usc.edu

Ming Hsieh Department of Electrical Engineering, University of Southern California, Los Angeles, CA, USA

Abstract—In this paper we demonstrate the capability of an ultra-wideband software defined radar (SDRadar) implemented in commercial USRP SDR hardware to produce high-resolution images of sub-surface landmine-like targets. We formulate a half-space back-projection focusing algorithm for low-altitude nadir-looking airborne altimetric ground-penetrating SAR that accounts for dispersive and refractive effects of the air-ground interface. Performance of the SDRadar and focusing algorithm are shown in experimental results. This work has applications in the development of low-cost high-resolution UAV-based radar systems for landmine detection and other sub-surface imaging tasks.

Keywords—Ground penetrating radar, software defined radar, UAV radar, frequency stacking, landmine detection

I. INTRODUCTION

The detection and removal of unexploded ordnance (UXO) and landmines is a significant international issue that poses extensive economic, political and technological challenges on a global scale [1]. The use of ground penetrating radar (GPR) has been explored extensively as a means of detecting landmines for more efficient clearance of mine fields left in civilian areas after cessation of previous conflicts. In general, landmines can be divided into three categories: metallic, minimum-metal, and non-metal and may be found on, just beneath, or far below the surface. The vast majority of damage to civilians is caused by small anti-personnel (AP) mines, such as the minimum-metal VS-50, which has a diameter of 9 cm [2]. This poses significant challenges to detection of land mines with GPR. A high bandwidth is required to obtain the resolution necessary to detect signatures from small targets. Further, target proximity to and rejection of strong surface returns creates additional difficulties. As noted by Daniels, "for the case of a weak target adjacent to a strong target [...] there is no accepted definition of resolution" [3].

The majority of current GPR landmine detection systems fall into two categories: vehicle based, such as the CSES HMDS, and handheld, such as the AN/PSS-14 [2]. A handful of airborne SAR-based systems have also been applied to this task. Feasibility studies in previous literature reports that for an airborne SAR system to reliably detect AP mines, a range resolutions of 5 cm is necessary; this would be obtained with ~ 3 GHz of instantaneous bandwidth coverage from 200 MHz to 3 GHz [2]. The Mineseeker System is a large airship-based side-looking UWB SAR that meets these requirements and has demonstrated the capability to detect minimum-metal AP land-mines [2].

The use of small rotor-based unmanned aerial vehicles (UAV)s and inexpensive sensors for AP landmine detection has the potential to significantly reduce cost, effort, time, and

risk associated with mine field clearance. However, in many cases radar systems capable of such resolution performance, in addition to being expensive, are too heavy and large to be carried as a small rotor-based UAV payload. This has led to interest in the use of small commercial software defined radio (SDR) platforms such as the Universal Software Radio Peripheral (USRP) platforms for such applications. Previously, a USRP SDR mounted on a UAV has been explored as a GPR for landmine detection in [4]. However, this work imposes the USRP sampling bandwidth of 56 MHz as a constraint on the signal bandwidth. This bandwidth is far below the widely accepted requirements for a system to reliably detect small landmines while rejecting false targets and surface clutter.

In this work, we demonstrate the capability of a UWB software defined radar (SDRadar) implemented in a small low-cost USRP SDR, as presented in [5], to image mine-like targets in the presence of surface clutter at a resolution < 8 cm. Further, we formulate a global time-domain back-projection focusing algorithm for a low-altitude nadir-looking altimetric rotor-based small UAV that accounts for the dispersive and refractive effects of electromagnetic wave propagation through the ground-air interface, herein referred to as half-space back-projection (HSBP).

II. HALF SPACE BACK-PROJECTION FOCUSING

The time-domain back-projection (BP) focusing algorithm is widely used in modern SAR systems due to the flexibility and precision with which phase and motion errors can be compensated and the high quality of images produced. While more computationally complex than other common SAR focusing algorithms, BP lends itself naturally to parallel processing and pre-computation [6] [7]. Modification of BP that account for refractive and dispersive effects encountered in ground-penetrating SAR have been explored previously for traditional side-looking SAR [8] [9] [10]. We formulate a similar correction of BP focusing specific to a low-altitude nadir-looking airborne altimetric ground-penetrating SAR.

Assuming an upper medium with known relative permittivity ϵ_{r1} and lower medium with known relative permittivity ϵ_{r2} and a radar platform at a known height h above the ground surface, we consider a sub-surface scatterer at a location (x_r, y_r, z_r) relative to the radar. Because the radar is operating as an altimeter, with an incidence angle normal to the ground surface, we will assume that the radar and scatterer lie within the same x, z plane such that $y_r = 0$. The imaging geometry is depicted in Figure 1. Illuminated sub-surface scatterers within the antenna beamwidth, β_a , will be subjected to changing refractive and dispersive effects as the antenna moves along the synthetic aperture. The optical path length or apparent

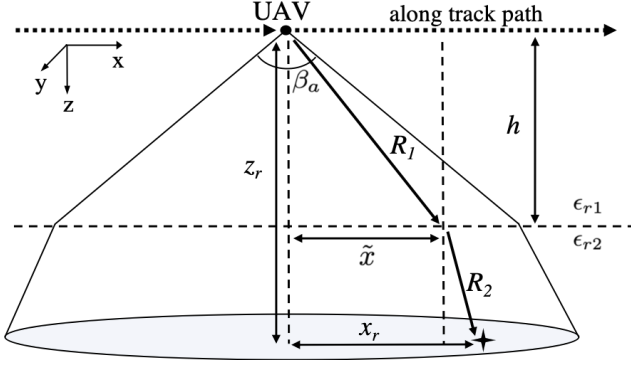


Fig. 1. Imaging geometry for an airborne nadir-looking SAR

free space range R_{fs} of contributions due to this sub-surface scattering feature is

$$R_{fs} = \sqrt{\epsilon_{r1}} \sqrt{h^2 + \tilde{x}^2} + \sqrt{\epsilon_{r2}} \sqrt{(z_r - h)^2 + (x_r - \tilde{x})^2} \quad (1)$$

where \tilde{x} is the half-space refractive point. On the basis of Fermat's principle, the optical path can be determined by differentiation of R_{fs} with respect to \tilde{x} , yielding a quartic equation of the form

$$\begin{aligned} & \tilde{x}^4 \left(1 - \frac{\epsilon_{r2}}{\epsilon_{r1}}\right) + \tilde{x}^3 \left[2x_r \left(\frac{\epsilon_{r2}}{\epsilon_{r1}} - 1\right)\right] + \tilde{x}^2 \left[x_r^2 + (z_r - h)^2\right] \\ & - \frac{\epsilon_{r2}}{\epsilon_{r1}} (h^2 + x_r^2) + \tilde{x} (2x_r h^2 \frac{\epsilon_{r2}}{\epsilon_{r1}}) - h^2 x_r^2 \frac{\epsilon_{r2}}{\epsilon_{r1}} = 0 \end{aligned} \quad (2)$$

Closed formed solutions to the general quartic equation can be found in [11].

We now define the half space back-projection (HSBP) algorithm as follows. Let l be an index variable for antenna locations along the aperture. Define the index variables n and m for along-track and range bins, respectively, in the raw image. For N_x antenna locations and N_r range bins, $l, n \in \{1, N_x\}$ and $m \in \{1, N_r\}$. If necessary, the received waveform is pulse-compressed in range at each step along the aperture.

For the l^{th} radar scan, the antenna is located at a position $(x_l, 0, 0)$ along the synthetic aperture. For each scan and for each complex pixel in the raw image, $d_{n,m}$, located at along track bin x_n and range bin r_m , we find the true pixel depth relative to the antenna, $z_{n,m}^l$ and the refractive point $\tilde{x}_{n,m}^l$, according to (1) and (2) by numerically solving

$$r_m = \sqrt{\epsilon_{r1}} \sqrt{h^2 + \tilde{x}_{n,m}^l{}^2} + \sqrt{\epsilon_{r2}} \sqrt{(z_{n,m}^l - h)^2 + (x_n^l - \tilde{x}_{n,m}^l)^2} \quad (3)$$

for $z_{n,m}^l$ and $\tilde{x}_{n,m}^l$, where $x_n^l = x_l - x_n$. We then correct the spatial doppler phase at each pixel to obtain $\tilde{d}_{l,m}$, accounting for dispersion and refraction by solving for the path lengths in medium 1 and 2, denoted as R_1 and R_2 respectively

$$R_1 = \sqrt{h^2 + \tilde{x}_{n,m}^l{}^2} \quad R_2 = r_m - R_1 \quad (4)$$

$$\tilde{d}_{l,m} = d_{l,m} \exp(j \frac{4\pi f_c}{c} (\sqrt{\epsilon_{r1}} R_1 + \sqrt{\epsilon_{r2}} R_2)) \quad (5)$$

We interpolate the $\tilde{d}_{l,m}$ pixels onto a uniform grid and accumulate the echoes in the n^{th} column of the HSBP focused image.

III. SIMULATION

We start by performing simulations using the open-source Finite-Difference Time-Domain (FDTD) electromagnetic simulation software GPRMax [12]. The simulation geometry is visualized in Figure 2. The simulated domain size is 5m x 0.01m x 6m with a spatial discretization of 1 cm and time step of 23.6 ps. The ground material is simulated as dry sand with a relative permittivity $\epsilon_r = 2.5$ and conductivity $\sigma_e = 0.0059$ S/m. The excitation pulse is a 600 MHz Ricker wavelet.

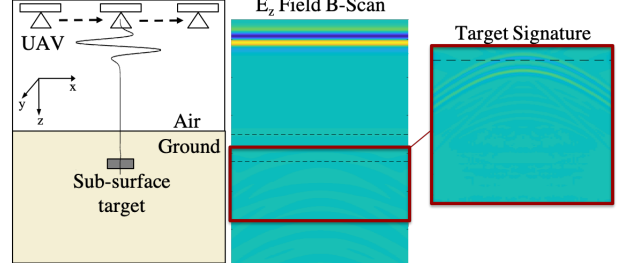


Fig. 2. Simulation scene geometry and B-Scan image

The TX/RX antenna is stepped across the simulation space in 5 cm increments to form a 5 m aperture at fixed height above the air-ground interface of 2.5 m. The 100 simulated A-scans are combined to form a two-dimensional B-Scan. The characteristic hyperbolic signature of sub-surface targets in a GPR B-Scan can be seen in Figure 2.

A. Metallic mine

We first simulate metallic AP mine-like targets as small PEC cylinders having radius 4.5 cm and height 4.5 cm buried parallel to the surface at a depth of 50 cm beneath the ground surface (BGS). We also simulate two PEC cylinders separated by 1 m, each with the same radius and depth. The raw B-Scan images are shown in Figure 3a and Figure 3b. The sub-surface targets appear as hyperbolic signatures, characteristic of B-Scan GPR images.

Focusing is first performed with conventional free-space BP, shown for the one and two PEC cylinder cases in Figures 3c and 3d respectively. Results obtained with the HSBP algorithm described in Section II for the each case are shown in Figures 3e and 3f. We observe that even for a relatively low contrast between the air and ground and a 50 cm target depth the dispersive and refractive effects have significant effect on the quality of the focused images.

B. Minimum metal mine

We now simulate a VS-50 style minimum metal AP mine buried at 10 cm and 50 cm BGS. The primary explosive component of the VS-50 is RDX. The impact of small internal metallic components and inclusions on the scattering of a minimum metal mine is minimal [3] and the electrical conductivity of plastics and explosives are typically near zero [13]. Accordingly we simulate the minimum metal mine as a dielectric disk having both a radius and height of 4.5 cm and with relative permittivity $\epsilon_r = 3.14$ and electrical conductivity $\sigma_e = 0.000059$ S/m. Focusing results for the simulated minimum-metal AP mines at depths of 10 cm and 50

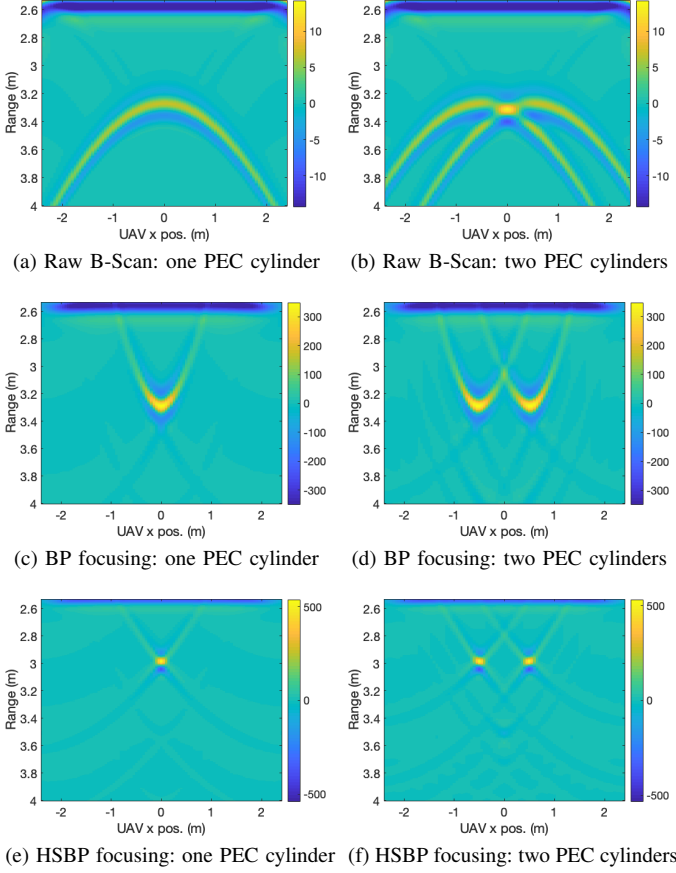


Fig. 3. Raw and focused B-Scan images obtained from simulation of one and two PEC mine-like cylinders buried at 50 cm BGS in dry sand.

cm are shown for BP in Figures 4a and 4b respectively. Results obtained with HSBP are given in Figures 4c and 4d. We omit images of raw B-Scans for this case. The visibility, localization and therefore likelihood of detection is improved by focusing, and by HSBP in particular. The two dielectric boundaries that occur at the upper and lower surfaces of the simulated mines are clearly visible in the focused target signatures.

IV. EXPERIMENTAL RESULTS

A. Hardware

The SDRadar sensor is implemented using a USRP E312 2x2 MIMO embedded battery-powered SDR from Ettus Research. The device has an Analog Devices AD9361 RF transceiver frontend capable of tuning frequencies from 70 – 6000 MHz with 54 MHz instantaneous bandwidth. A USB WIFI module is added for wireless data acquisition and remote control. The Tx/Rx antennas are UWB Vivaldi antennas from RFSpace capable of operating from 600 – 6000 MHz. A detailed description of the SDRadar system can be found in [5]. The entire radar weighs < 1 kg and is shown suspended from a fixed line above the test site in Figure 5. Preliminary flight testing with the system mounted on a DJI S1000 octocopter UAV has confirmed its suitability as a sensor payload.

We operate the SDRadar in a non-uniform stepped-frequency mode, transmitting a $36 \mu\text{s}$ 50 MHz bandwidth LFM

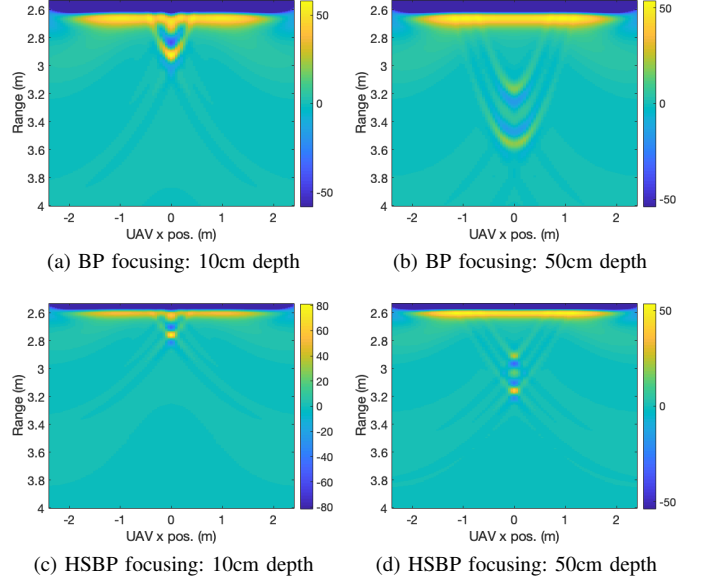


Fig. 4. BP and HSBP focused B-Scans for simulated VS-50 style minimum-metal AP mine buried at 10 cm and 50 cm BGS in dry sand.

waveforms coherently at each of 105 steps from 600 MHz to 3.1 GHz for a total bandwidth (BW_t) of 2.5 GHz. The frequency stacking algorithm presented in [5] is used coherently combine the sub-pulses to obtain the high-resolution synthetic wide-band waveform (SWW) scans presented herein. The free space range resolution of the system is 6 cm.

B. Experiment Setup

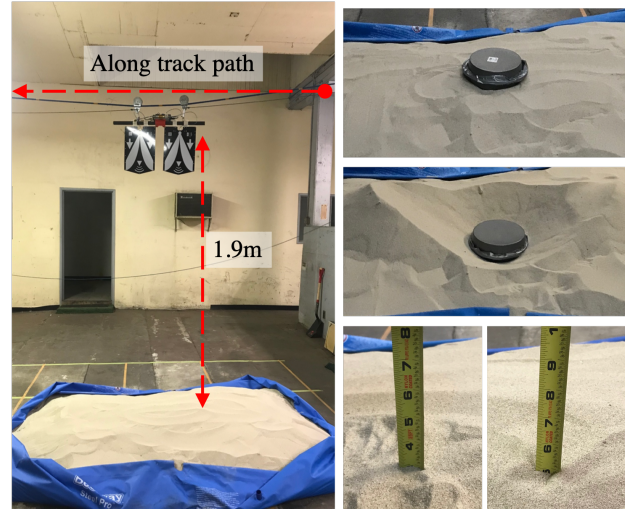


Fig. 5. **Left:** Experimental Setup with no target present. **Top right:** Metallic mine-like target on ground surface. **Middle right:** Metallic mine-like target placed 8 cm BGS uncovered. **Bottom right:** Measurements of buried target depths: 7.62 cm (3 in.) and 12.7 cm (5 in.) BGS

The test site consists of a $2.388\text{m} \times 1.4986\text{m} \times .5842\text{m}$ plastic pool filled with $.7646 \text{ m}^3$ of fine grain sand; an average sand depth of 21.3 cm. We suspend the radar sensor above the sand pool from a taut fixed line such that the distance from the sensor to the sand surface was $\sim 1.9 \text{ m}$. Movement of the radar in the along-track direction was controlled manually

using a pulley system. A simple cylindrical target with radius of ~ 15 cm and height of ~ 10 cm was constructed from two aluminum pans to simulate a medium size metallic mine. We assume that the sand has a relative permittivity of $\epsilon_r = 2.5$.

We form a 1.5 m synthetic aperture with a spatial sampling interval of 10 cm. The SAR imaging is performed in a ‘stop and go’ fashion, wherein the radar remains motionless for a duration of ~ 10 s while each A-scan is completed, with movement to the next position in the aperture occurring between pulses. In a rotor-based UAV, this is equivalent to hovering at a waypoint before proceeding the next.

C. Imaging Results

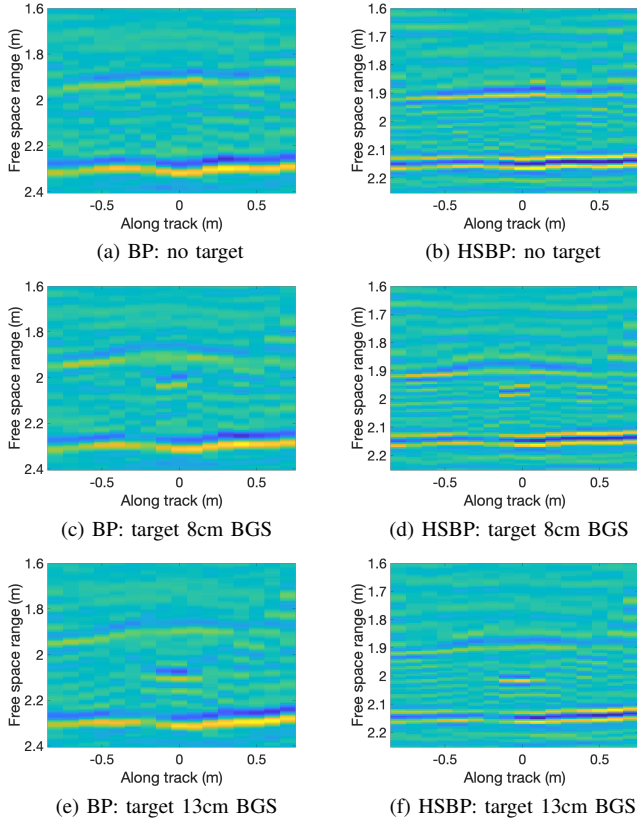


Fig. 6. Focused GPR B-scan imaging results across 1.5 m aperture with metallic-mine like target on ground surface and at 8 cm and 15 cm BGS.

We present GPR imaging results for three scenarios: (i) the test site with no target present (Figures 6a, 6b), (ii) a target buried at a depth of 8 cm BGS (Figures 6c, 6d), and (iii) a target buried at 13 cm BGS (Figures 6e, 6f). For each case, we plot focused images obtained with free-space BP and with HSBP. The surface returns from the sand layer and concrete below appear clearly in all images. We note that in the HSBP focused images, the span of the free space range/ depth axes are decreased so that features are more easily compared across all images. In the HSBP focused images, the free space range is representative of true spatial depth. Target depth measurements are given for each focusing mode in table I. Values are obtained via peak detection from the depth profile at the center of each aperture.

TABLE I. MEASURED SUB-SURFACE TARGET DEPTHS AFTER FOCUSING

Focusing algorithm	Measured Depth BGS (cm)		
	Sand bottom	Target 8 cm	Target 13 cm
BP	38.8	14.7	19.4
HSBP	23.5	10.0	12.9
Ground truth	21.3	7.62	12.7

V. CONCLUSION

In this work, we have developed a method for high resolution imaging of mine-like targets buried at shallow depths. This method was demonstrated as a new capability of our USRP SDR-based UWB SDRadar. We developed a SAR focusing algorithm that corrects dispersive and refractive effects, formulated for a nadir-looking air-borne GPR. We verified the algorithm performance in simulation and experiment. Future research directions include (i) integrating the system on a UAV platform and imaging sub-surface targets in flight tests, (ii) imaging of smaller and minimum-metal mine-like targets, (iii) optimization and parallelization of the HSBP algorithm for imaging on embedded platform and (iv) mine detection and ground surface tracking algorithms for automated detection.

REFERENCES

- [1] G. Tesfamariam and D. Mali, “GPR Technologies for Landmine Detection,” *TECHNIA - International Journal of Computing Science and Communication Technologies*, vol. 5, July 2012.
- [2] D. J. Daniels, “A review of GPR for landmine detection,” *Sensing and Imaging: An International Journal*, vol. 7, pp. 90–123, Sept. 2006.
- [3] D. J. Daniels, “Ground penetrating radar for buried landmine and IED detection,” in *Unexploded Ordnance Detection and Mitigation*, pp. 89–111, Springer, 2009.
- [4] M. R. P. Cerquera, J. D. C. Montaña, and I. Mondragón, “UAV for Landmine Detection Using SDR-Based GPR Technology,” in *Robots Operating in Hazardous Environments* (H. Canbolat, ed.), InTech, Dec. 2017.
- [5] S. Prager, T. Thrivikraman, M. Haynes, J. Stang, D. Hawkins, and M. Moghaddam, “Ultra-wideband synthesis for high-range resolution software defined radar,” in *2018 IEEE Radar Conference (Radar-Conf18)*, pp. 1089–1094, April 2018.
- [6] R. Bamler, “A comparison of range-Doppler and wavenumber domain SAR focusing algorithms,” *IEEE Transactions on Geoscience and Remote Sensing*, vol. 30, pp. 706–713, July 1992.
- [7] L. A. Gorham and L. J. Moore, “SAR image formation toolbox for MATLAB,” p. 769906, Apr. 2010.
- [8] M. Albahkali and M. Moghaddam, “3d sar focusing for subsurface point targets,” in *2009 IEEE International Geoscience and Remote Sensing Symposium*, vol. 1, pp. 1–60–I–63, July 2009.
- [9] T. Jin and Z. Zhou, “Refraction and Dispersion Effects Compensation for UWB SAR Subsurface Object Imaging,” *IEEE Transactions on Geoscience and Remote Sensing*, vol. 45, pp. 4059–4066, Dec. 2007.
- [10] J. Fortuny-Guasch, “A novel 3-D subsurface radar imaging technique,” *IEEE Transactions on Geoscience and Remote Sensing*, vol. 40, no. 2, pp. 443–452, Feb./2002.
- [11] M. Abramowitz and I. A. Stegun, “Solutions of quartic equations,” in *Handbook of Mathematical Functions with Formulas, Graphs, and Mathematical Tables*, ch. 3.8.3, pp. 17–18, New York NY: Dover, 9 ed., 1972.
- [12] C. Warren, A. Giannopoulos, and I. Giannakis, “An advanced gpr modelling framework: The next generation of gprmax,” in *2015 8th International Workshop on Advanced Ground Penetrating Radar (IWAGPR)*, pp. 1–4, July 2015.
- [13] F. Roth, P. van Genderen, and M. Verhaegen, “Radar Response Approximations For Buried Plastic Landmines,” in *SPIE*, vol. 4758, SPIE, 2002.